Ceramics International 44 (2018) 2982–2990

Contents lists available at ScienceDirect

Ceramics International

journal homepage: www.elsevier.com/locate/ceramint

Sintering characteristics of plasma-sprayed TBCs: Experimental analysis and an overall modelling

Guang-Rong Li, Guan-Jun Yang*, Cheng-Xin Li, Chang-Jiu Li

State Key Laboratory for Mechanical Behaviour of Materials, School of Materials Science and Engineering, Xi'an Jiaotong University, Xi'an, Shaanxi Province 710049, PR China

ARTICLE INFO

Keywords:
Thermal barrier coatings (TBCs)
Plasma spray
Sintering
Stage-sensitive kinetics
Structural tailoring

ABSTRACT

In this study, sintering behaviour of plasma-sprayed thermal barrier coatings (PS-TBCs) was investigated experimentally and theoretically. Results show that the sintering kinetics of PS-TBCs is highly stage-sensitive. The sintering proceeds significantly faster at initial short thermal exposure (< 20 h), while it slows down dramatically at following long thermal exposure. A detailed examination on microstructural evolution of the PS-TBCs was carried out to understand their sintering behaviour. Results show that, different from the conventional sintering theory, the healing of 2D pores was dominantly responsible for the stage-sensitive sintering kinetics during thermal exposure. In brief, the sintering characteristics of the PS-TBCs are highly structure specific. In addition, a structural model was developed based on the structural characteristics of the PS-TBCs; and the model predicts a well consistent sintering behaviour with experiments. Finally, an outlook towards TBCs with higher performance was put forward.

1. Introduction

The proliferated use of films or coatings meets the diverse and special requirements, like corrosion, wear-resistance [1–3], thermal-insulation [4] and others [5]. As a representative example, thermal barrier coatings (TBCs) are widely used in both aircraft engines and land-based gas turbines to protect the metal components in hot-section. The TBCs exhibit excellent performance of thermal insulation at high temperature [6,7]. Therefore, the efficiency of gas turbines is improved notably, owing to the fact that the TBCs enable higher operating temperatures in hot section. Typically, the thermal barrier effect and the resistance to spalling exposed to high temperature are two key performances of TBCs [8]. These performances are highly dependent on features of the coating microstructure. Therefore, it is important to understand the microstructural evolution of TBCs during thermal exposure.

Commonly, a TBC consists of an oxidation-resistant bond-coat and a thermal-insulating top-coat. The high thermal resistivity of the top-coat depends dominantly on the unique porous structure inherent to the thermal spray process. During the process of thermal spraying, a stream of molten or partially molten particles impacts on substrate followed by lateral flattening, rapid solidification and cooling [9,10]. Consequently, a thermally-sprayed coating often exhibits a lamellar microstructure with inter-splat pores, intra-splat cracks and globular voids [11–13]. The inter-splat pores, oriented normally to the heat flux direction, generally refer to the imperfect bonding between splats [13,14]. The intra-splat microcracks often run through the thickness of the individual splats [11,14]. Moreover, the inter-splat pores and the intra-splat cracks are connected to form a 2-dimensional (2D) pore network [15,16]. For conventional porous structure, porosity is widely used to characterize the structure [17,18]. However, in the case of the thermally-sprayed coatings, the porosity is often about 10∼15% [19,20], whereas the thermal [13,15,21–23] and mechanical [24–28] properties are only approximately < 50% with respect to those of the bulk materials. Therefore, the 2D pore network may dominantly determine the performance of the thermally-sprayed top-coat.

Significant increases of the thermal conductivity [13,19,29–32] and the elastic modulus [13,19,24,32–34] were observed during thermal exposure. Regarding the structural evolution, most investigations focused on the global changes, e.g., changes in linear shrinkage [35] and porosity [13]. However, the changes in porosity are much less than those in the thermal and mechanical properties. Some reports revealed qualitatively the inter-splat locking and the splat stiffening [29,30]. Nevertheless, it is still difficult to understand the performance degradation, since the relationship between the 2D pore healing and the property evolution remains unknown. Therefore, it is highly necessary to investigate quantitatively the healing behaviour of the 2D pore, and to correlate the essential microstructural changes with the property

* Corresponding author.
E-mail address: ygj@mail.xjtu.edu.cn (G.-J. Yang).

https://doi.org/10.1016/j.ceramint.2017.11.052
Received 12 September 2017; Received in revised form 30 September 2017; Accepted 8 November 2017
Available online 10 November 2017

Table 1
Parameters used for APS YSZ.

Parameter	Unit	Value
Plasma arc voltage	V	70
Plasma arc current	A	600
Flow rate of primary gas (Ar)	L/min	50
Flow rate of secondary gas (H_2)	L/min	7
Flow rate of powder feeding gas(N_2)	L/min	7
Spray distance	mm	110
Torch traverse speed	mm/s	800

evolution.

In this work, to begin with, changes in the mechanical property during thermal exposure were determined. Subsequently, a detailed pore healing behaviour was carried out to reveal the microstructural evolution induced by sintering. Based on the experimental findings, a quantitative structural model was developed to correlate the microstructural evolution with the changes in mechanical property.

2. Experimental

2.1. Sample preparation

Commercially available hollow spheroidized 8 wt% YSZ powders (HOSP, −75 to +45 μm, Metco 204B-NS, Sulzer Metco Inc., New York, USA) were used to prepare the top-coat. YSZ coatings with a thickness of 500 μm were deposited on a stainless-steel substrate using a commercial plasma spray system (GP-80, 80 kW class, Jiujiang, China). The top-coat can thereby be termed as PS-YSZ. The spray parameters are shown in Table 1. Free-standing YSZ coatings were obtained through post-spray dissolution of the substrate by a hydrochloric acid solution, following by further immersing in deionized water for 24 h to remove the residual acid in coatings.

2.2. Thermal exposure for samples

In order to examine the microstructural and property evolution of YSZ coatings during thermal exposure, free- standing samples were heated in a furnace to the temperatures of 1150 °C. After progressively holding for different durations, the samples were cooled down to room temperature. In order to avoid unexpected coating structure degradation by fast temperature change, the heating rate and the cooling rate were fixed at a relatively low rate of 10 °C/min. Based on previous reports [34,36], the significant formation of monoclinic phase often occurs at higher temperatures above 1200 °C. Therefore, it is reasonable to conclude that the sintering at 1150 °C is relatively unaffected by the phase change.

2.3. Structural characterization and property determination

Surface and cross-sectional morphologies of the YSZ coatings were examined using scanning electron microscope (SEM, TESCAN MIRA 3, Czech). Quasi in-situ observation for the healing of 2D pores was carried out using the SEM, as shown in Fig. 1. The detailed procedure can be described as follows: (i) a sample with the dimensions of Φ20 × 0.5 mm was fractured roughly along its diameter (A-A′). The observations of the inter-splat pores and the intra-splat cracks were conducted on the cross-section and surface, respectively; (ii) In the case of the inter-splat pores, a targeted pore was firstly found from the cross-section at a high magnification (see the red dot in Fig. 1b). Subsequently, the magnification was decreased gradually until the global sample morphology can be observed. The position of the red dot can be fixed by measuring the L_1 and T_1. After thermal exposure, the corresponding position was obtained at a lower magnification. Subsequently, the magnification was increased to the required magnification; (iii) In the case of the intra-splat cracks, a 1/4 sample was used in this study, as shown in Fig. 1c. Similar to the observation of the inter-splat pores, the corresponding coordinate (L_2 and T_2) of the targeted position was obtained for the quasi in-situ observation.

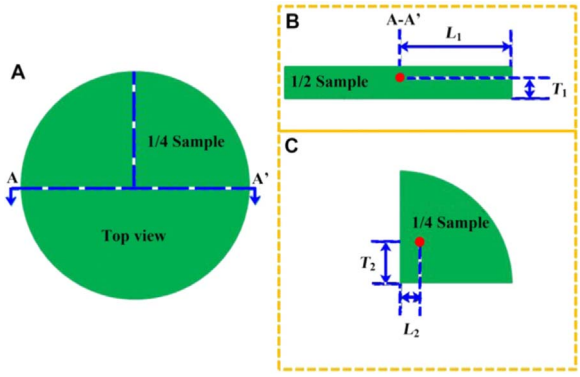

Fig. 1. Schematics for the quasi in-situ observation: (a) a global top view of the sample; (b) observation for the inter-splat pores; and (c) observation for the intra-splat cracks. (For interpretation of the references to color in this figure legend, the reader is referred to the web version of this article.)

The apparent porosity of the coatings was determined by the image analysis using the SEM at a magnification of 1000×. At least ten images were used to estimate the porosity of each sample. It is known that the 2D pores essentially determine the thermal and mechanical properties [15,37] of the top-coat. Accordingly, 2D pore density, defined as the total length of 2D pores in unit area, was also determined in the present work. Some other details to determine the 2D pore density can be found elsewhere [37].

The macroscopic elastic modulus (E) were determined using a three-point bending (3PB) test system (Instron 5943, America) [38]. The sample dimensions were 60 × 10 × 0.5 mm. The E can be obtained from the following formulas:

$$w = \frac{PL^3}{48D} \tag{1}$$

$$D = \frac{Eh^3}{12(1-\nu^2)} \tag{2}$$

where P is the load applied to the middle of the span, L is the span between two supports, D is the bending stiffness, E is the elastic modulus of the coating, h is the coating thickness, ν is the Poisson's ratio of the coating.

The microscopic elastic modulus were determined using a Knoop indentation test system (Buehler Micromet 5104, Akashi Corporation, Japan). The test was performed at a load of 300 g and holding time of 30 s. The sample dimensions were Φ20 × 0.5 mm. Knoop indentation is based on the measurement of the elastic recovery of the in-surface dimensions of then indentations [25]. During unloading, the elastic recovery reduces the length of the minor diagonal of the indentation impression (b'), whereas the length of the major diagonal of the indentation impression (a') remains relatively unaffected. The in-plane elastic moduli was determined from the polished surface of the coating samples. In contrast, the out-plane elastic moduli was obtained from the polished cross-section, making sure that the minor diagonal was parallel to the deposition direction. The formula for determining the elastic modulus is:

$$E = \frac{\alpha H}{(\frac{b}{a} - \frac{b'}{a'})} \tag{3}$$

where α is a constant (0.45), H is hardness, a' and b' are the lengths of the major and minor diagonals of the indentation impression, respectively, and b/a is 1/7.11.

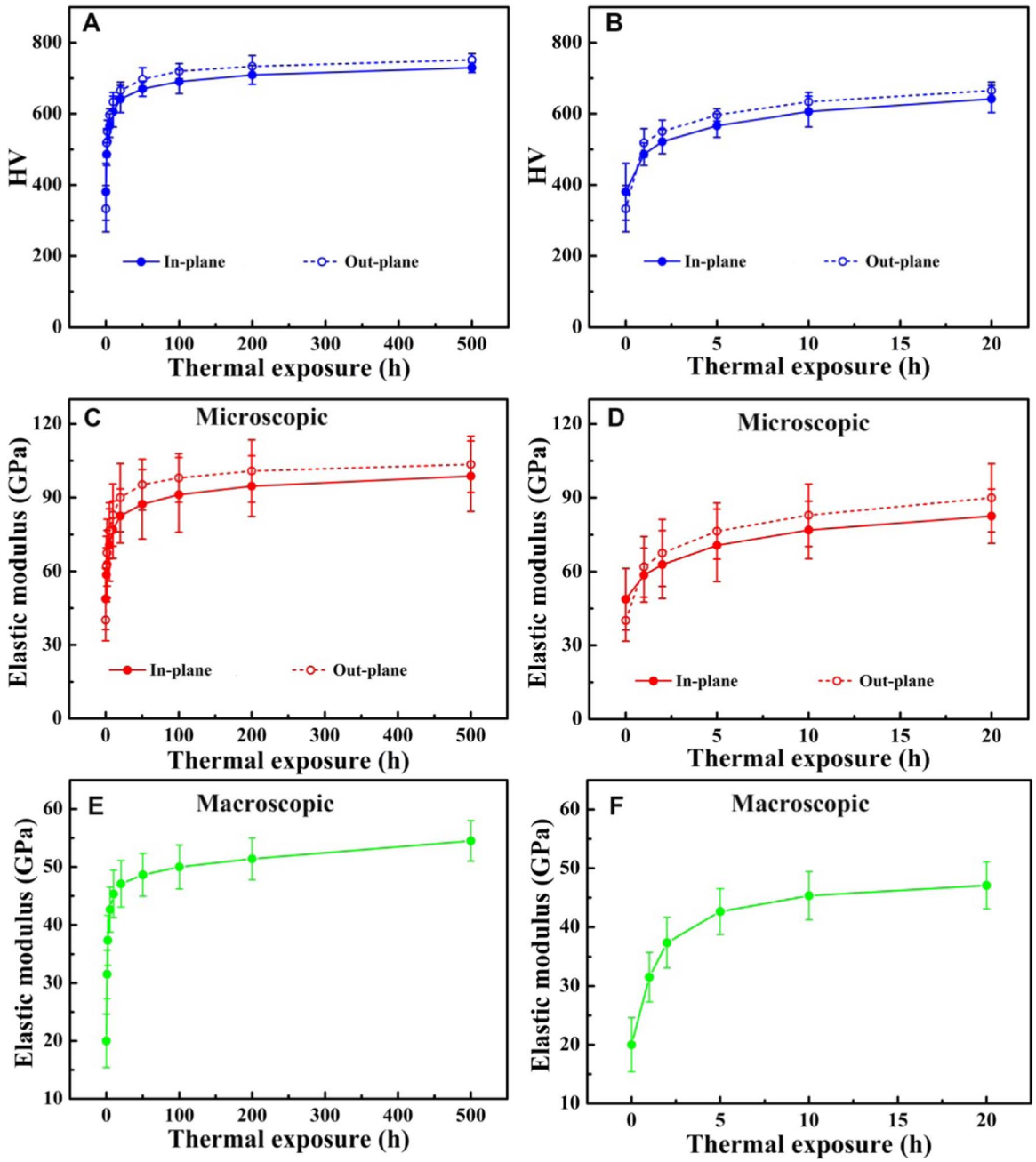

Fig. 2. Changes in mechanical properties as a function of thermal exposure duration: (a) hardness for 500 h; (b) hardness for 20 h; (c) microscopic elastic modulus for 500 h; (d) microscopic elastic modulus for 20 h; (e) macroscopic elastic modulus for 500 h; and (f) macroscopic elastic modulus for 20 h.

3. Experimental results and discussion

3.1. Overall evolution of the microstructure and the mechanical properties

Fig. 2 shows changes in the mechanical properties as a function of thermal exposure duration. It can be found that the mechanical properties exhibit significant increases, despite in microscale or macroscale. Moreover, the evolution exhibits an obvious non-linear trend. The increase was very fast at initial short duration, whereas it slowed down dramatically in the following long duration. Consequently, the initial short duration finished most increment with respect to that in whole duration, as shown in Fig. 2(b, d, f). This non-linear change is consistent with previous reports [13,19,24,30–34]. After long thermal exposure, the mechanical properties in different directions step closer, suggesting that the initial anisotropic state was gradually weakened due to sintering.

Fig. 3 shows the global structural evolution from the view of the polished cross-section. An obvious phenomenon is that the large-sized pores (approximately 5–15 μm) were decreased during thermal exposure. However, this apparent phenomenon cannot stand for the real response inside the coatings during sintering. It is reported that the visualized large-sized pores in cross-section primarily result from the spalling off of the weakly bonded splats during sample preparation [39,40]. At as-deposited state, plasma-sprayed ceramic coatings exhibit approximately 30% bonding ratio between splats [12]. During thermal exposure, the inter-lamellar bonding is enhanced induced by pore healing. Consequently, the spalling off of the splats would become difficult after thermal exposure. Therefore, the apparent change in Fig. 3 actually reflected an increasingly enhanced inter-lamellar bonding ratio. Fig. 4 shows the change in porosity as a function of

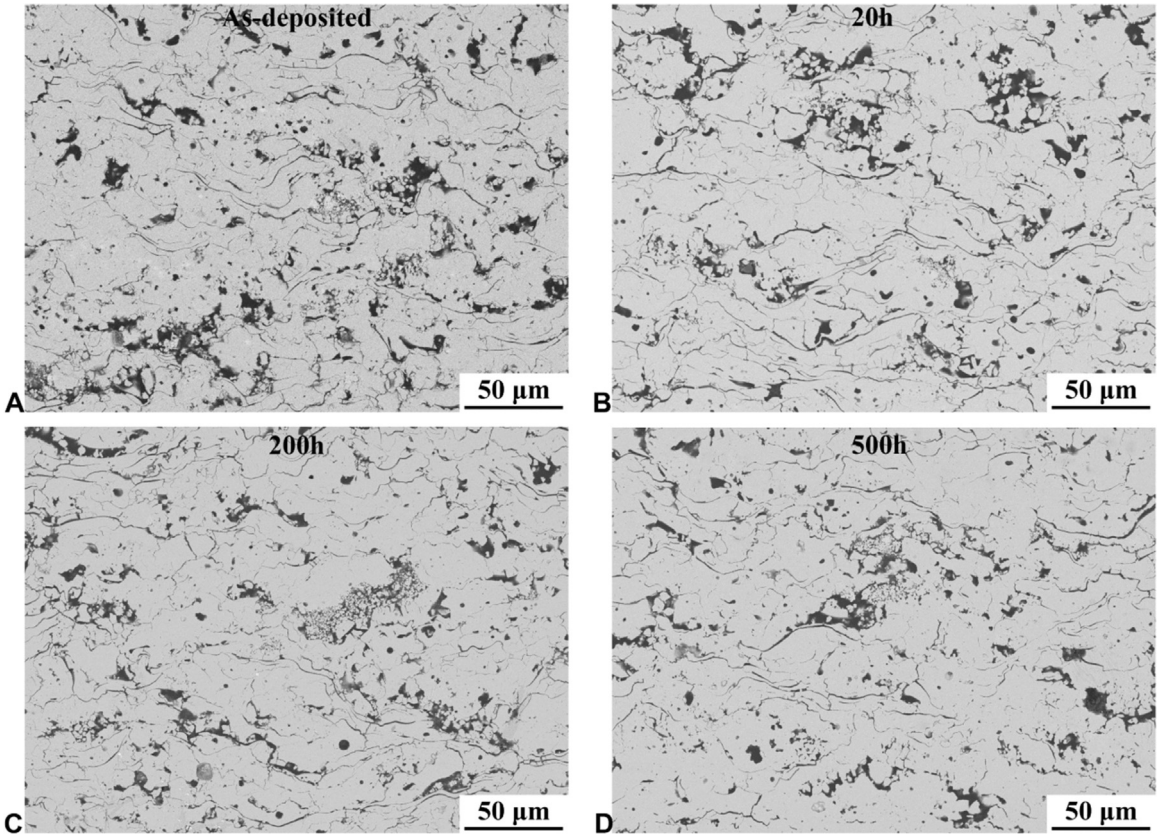

Fig. 3. Structural evolution as a function of thermal exposure duration: (a) as-deposited state; (b) 20 h; (c) 200 h; and (d) 500 h.

thermal exposure duration. It is obvious that the change scale of the apparent porosity is much smaller than that of the mechanical properties. Based on the discussion above, it can be confirmed that the apparent porosity is not essentially appropriate to characterize the structure evolution of the top-coat.

3.2. Stage-sensitive and anisotropic evolution of the mechanical properties

Fig. 5 shows the changes in mechanical properties presented by Ln-t curves. 0.1 h was used to stand for the as-deposited state. It can be found that the non-linear trends were transformed into nearly linear trends. Moreover, the total evolution was divided into two stages approximately, referred to as stage-I and stage-II. The divided boundary is located around 20 h, which is consistent with the shrinkage results [33]. It is obvious that the increment slope at the stage-I was much larger than that in the stage-II. Fig. 6 shows the increment and increase rate of the mechanical property in these two stages. It can be observed that the stage-I finished most increment in a few initial hours.

It is worth noting that the PS-YSZ coating exhibits obvious anisotropic properties at its as-deposited state. The mechanical property in the in-plane direction is larger than that in the out-plane direction [27,41]. However, after the stage-I, the mechanical properties in the out-plane direction exceeded those in the in-plane direction. It is reported that the mechanical property is more sensitive to its corresponding vertical cracks [42]. The anisotropic evolution trend may suggest that the healing rates of the 2D pores are different during thermal exposure.

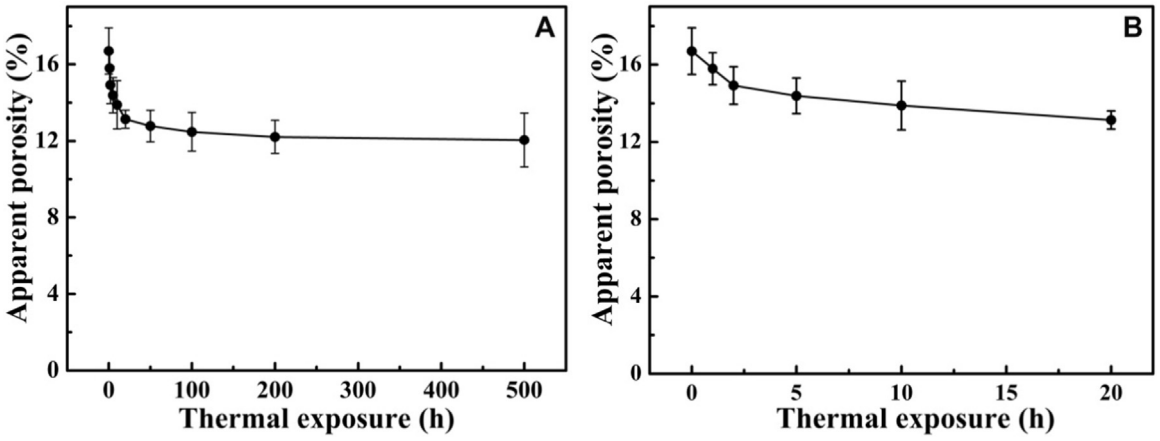

Fig. 4. Evolution of porosity as a function of thermal exposure duration: (a) 500 h and (b) 20 h.

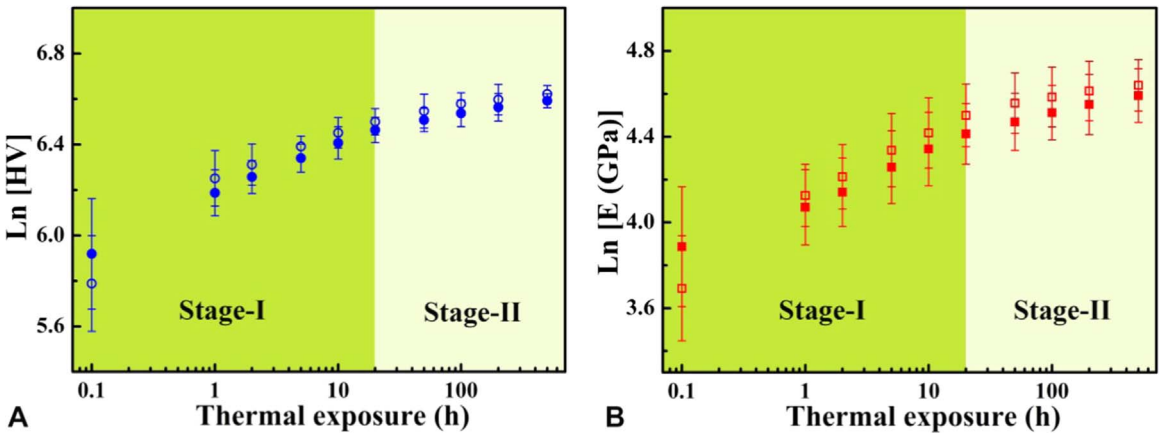

Fig. 5. Stage-sensitive evolutionary trend of the mechanical properties: (a) hardness and (b) microscopic elastic modulus.

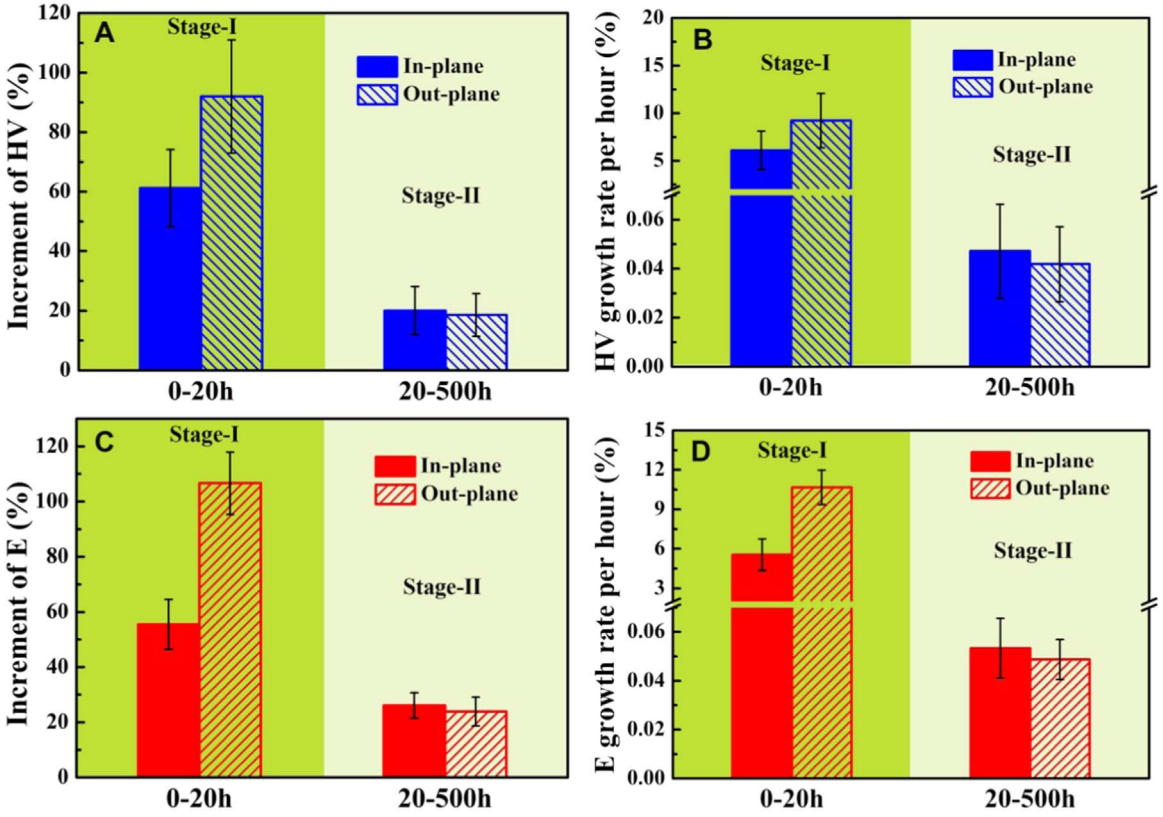

Fig. 6. Increment and increase rate of the mechanical property in two stages. (a) Increment of the hardness; (b) Increase rate of the hardness; (c) Increment of the microscopic elastic modulus; (d) Increase rate of the microscopic elastic modulus.

3.3. 2D pore healing behaviour related to the stage-sensitive sintering kinetics

Based on the changes in mechanical properties during thermal exposure, the stage-sensitive and anisotropic sintering kinetics were the main sintering features for the top-coat. Owing to the fact that the 2D pores dominantly determine the performance of PS-YSZ, the healing of 2D pores would be investigated in this section. Fig. 7 shows the healing procedure of inter-splat pores and intra-splat cracks. In the case of the inter-splat pores, it can be observed that the initial smooth splat surface became roughening after thermal exposure. This is consistent with previous report [43]. The healing of inter-splat pores mainly starts from the pore tips and proceeds by apparent bridge-connection due to the surface roughening. Moreover, the healed narrow part decreased the space of wide part, which increased the possibility of wide part to heal by bridge-connection. In the case of the intra-splat cracks, the healing was not so obvious after the stage-I. Fig. 8 shows the changes in 2D pore density as a function of thermal exposure duration. From the view of overall thermal exposure duration, both the densities of the inter-splat pores and the intra-splat cracks decreased dramatically compared with the apparent porosity (see Fig. 4), suggesting that the healing of 2D pores plays a dominant role on properties evolution. Moreover, it is possible to observe that the pore healing is also stage-sensitive. At the stage-I, the density of the inter-splat pores decreased much faster, whereas the density of the intra-splat cracks seems unaffected. At the stage-II, both the inter-splat pores and the intra-splat cracks decreased in a similar but much slower rate.

In brief, the ultrafast sintering kinetics at the stage-I is mainly attributed to the fast healing of inter-splat pores. Subsequently, at the stage-II, the healing rates of the inter-splat pores and the intra-splat

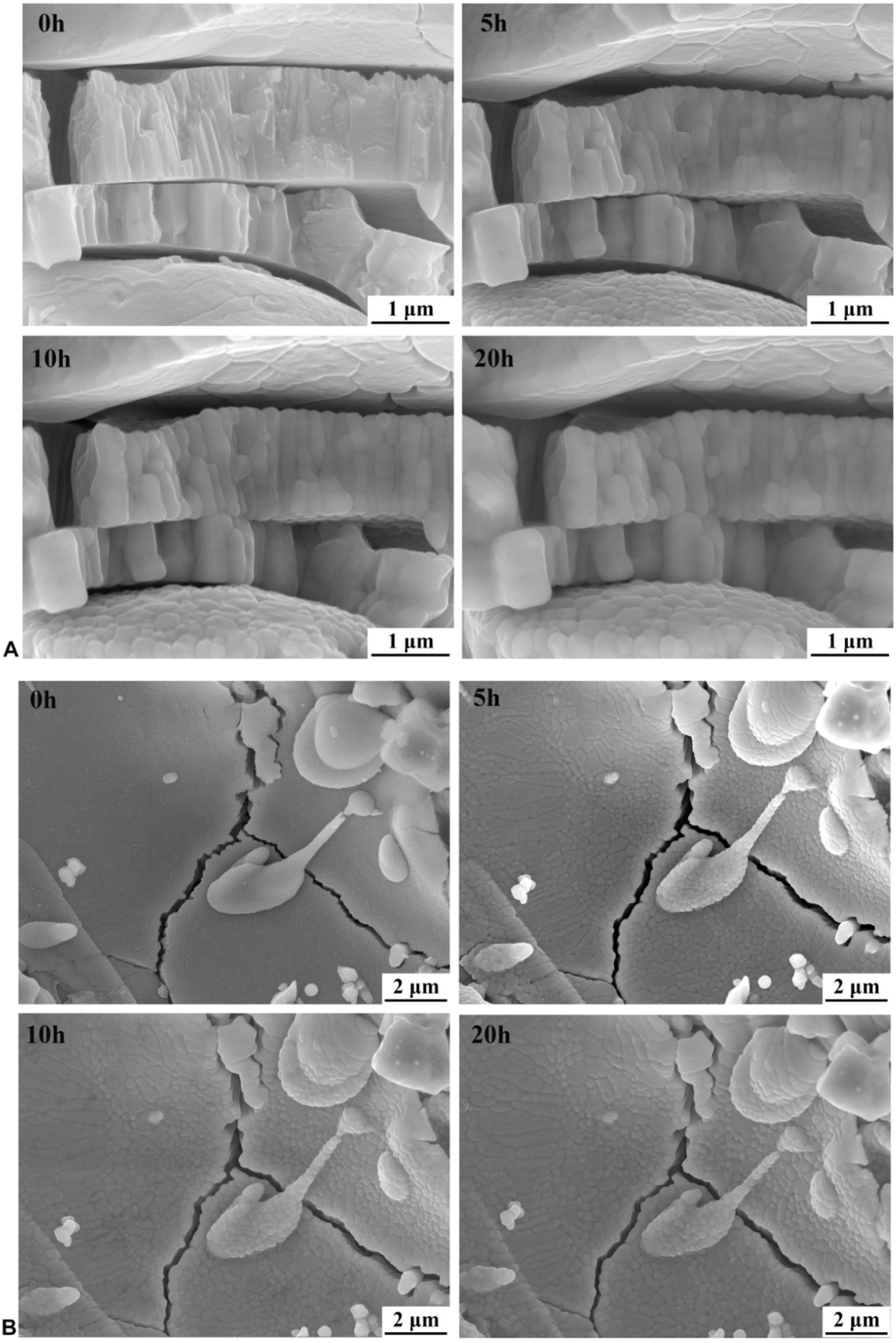

Fig. 7. Healing of the 2D pores during thermal exposure: (a) inter-splat pores and (b) intra-splat cracks.

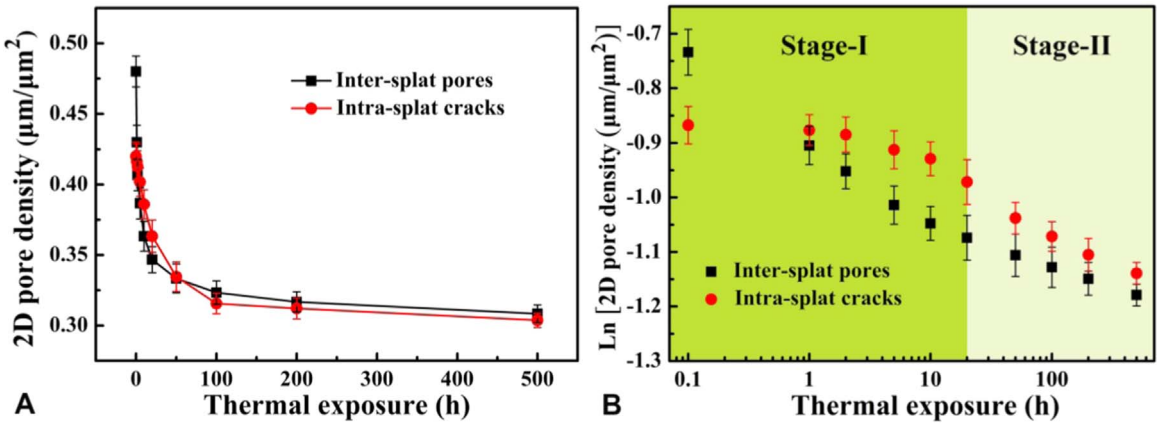

Fig. 8. Evolution of 2D pore density during thermal exposure: (a) evolution during different durations and (b) evolution of 2D pore density shown by Ln-t.

cracks slow down. The anisotropic pore healing behaviour can account for the phenomenon that the increase rate of mechanical properties in the out-plane direction exceed that in the in-plane direction. The sintering process of the PS-YSZ is driven by the decrease of free energy of the whole system. The sintering would proceed by the matter transfer. The roughening of the splat surface leads to the multi-connection of the counter-surface, which accelerates the matter transfer through multi-way diffusion. Consequently, a much higher sintering kinetic occurs at the stage-I. The inter-splat pores often correspond to the partial separated region between splats, whereas the intra-splat cracks result from the totally cracking behaviour [14,16]. As a result, the inter-splat pores exhibit a larger quantity of very narrow parts (pore tips) compared with that of the intra-splat cracks. That's why the multi-connection induced fast healing at the stage-I often occurs on the inter-splat pores. In the stage-II, the possibility of multi-connection decreases, and then the bonding area would be the only way to transfer matter. Consequently, the sintering kinetics slows down significantly. This is similar to that observed in conventional ceramic sintering [44], in which the neck between particles is the only way to transport materials and the neck diameter becomes larger and larger.

3.4. Correlation between microstructural evolution and mechanical property

The sintering characteristics of the PS-YSZ can be concluded as follows: (i) the change in mechanical property as a function of thermal exposure duration is stage-sensitive; (ii) at the stage-I, the ultrafast sintering kinetics is attributed primarily to the healing of inter-splat pores through multi-connection of the counter-surfaces. This is the unique sintering characteristic of the PS-YSZ; (iii) at the stage-II, the healing of inter-splat pores and intra-splat cracks would proceed through single-connection of bonding area. This is similar to the conventional ceramic sintering. The healing of inter-splat pores leads to increase of the inter-splat bonding ratio, which could be used to correlate the microstructural evolution with the mechanical property.

The inter-splat bonding ratio could be obtained from inter-splat pore density through the following formula [37,45]:

$$L_2 = \frac{HL_1}{\delta} \tag{4}$$

$$\varepsilon = \frac{\xi HL_1}{L_2} = \xi\delta \tag{5}$$

$$\alpha = (1 - \varepsilon) \times 100\% \tag{6}$$

where H and L_1 refer to the coating thickness and length, respectively. L_2 is the whole length of interface between splats in the coating, δ is the mean splat thickness, ξ is the residual 2D pore density, ε is the unbonded ratio contributed by 2D pores, and α is the bonding ratio.

The Eq. (4) describes the same area between the structure with stacked layers and the structure with spreading layers. The Eq. (5) describes the length ratio of the inter-splat pores (ξHL_1) with respect to the total interfacial length (L_2). Owing to the 2D shapes of the inter-splat pores, this length ratio is actually the unbonded ratio. Consequently, the bonding ratio can be obtained. In order to get the evolution of the bonding ratio from Eqs. (1)–(3), it is necessary to firstly obtain the mean thickness of splats and the as-deposited bonding ratio. In our

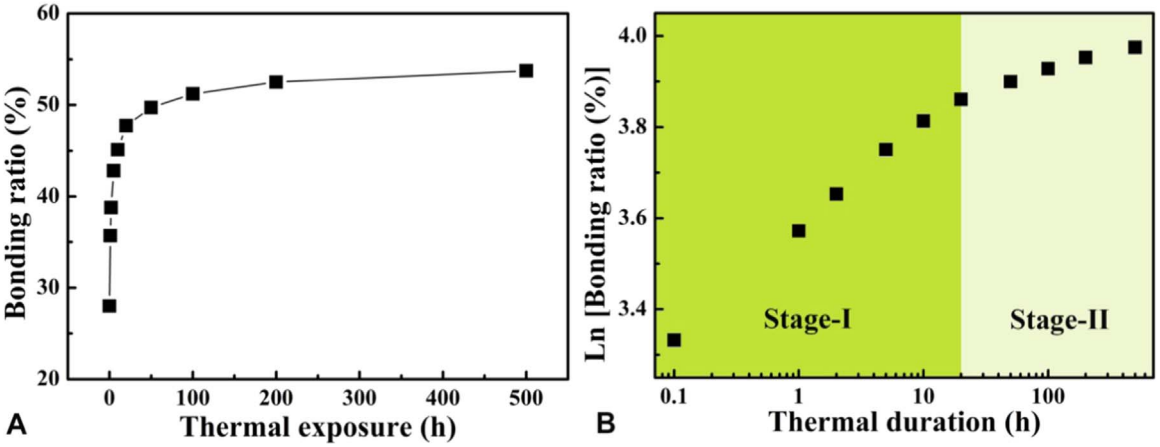

Fig. 9. Evolution of bonding ratio obtained from the 2D pore density during thermal exposure: (a) evolution of bonding ratio and (b) bonding ratio evolution presented by Ln-t corresponding to (a).

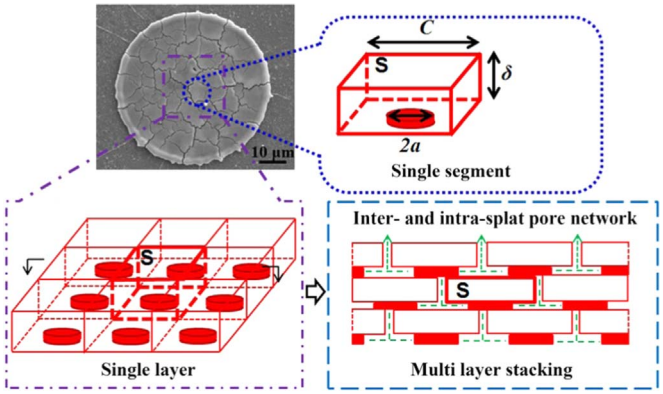

Fig. 10. The developed structural model based on PS-YSZ coatings.

previous report [16], the splat thickness and the mean bonding ratio has been determined to be 1.5 μm and 28%, respectively. This is consistent with other reports [9,12,45,46]. Fig. 9 shows the evolution of bonding ratio obtained from Eqs. (1)–(3). Similar to the changes in mechanical properties, a sharp increase could be observed at the stage-I. Moreover, the change in bonding ratio also appears to be stage-sensitive.

In order to correlate the microstructural evolution with mechanical property, a structural model based on the PS-YSZ coatings could be developed. It is well known that the PS-YSZ coatings are composed of multi-stacking layers with connected inter- and intra-splat pore network [11,13,16]. Moreover, the inter-splat pores are often perpendicular to the deposition direction, whereas the intra-splat cracks usually run vertically along the deposition direction. Therefore, the basic unit composing the whole coating is the individual segments divided by intra-splat cracks. Based on the experimental observation above, the developed structural model is shown in Fig. 10. The assumptions are as follows: (i) the segments are assumed to be cubic shape, termed as structural units; (ii) the bonded area is located at the bottom center of structural units. The bonding ratio can be determined by the area ratio of circular bonding region with cubic structural unit; (iii) the whole structure is formed by the stacking of structural units; (iv) at the stage-I, the healing of intra-splat cracks is neglected, while at the stage-II, the healing of inter-splat pores and intra-splat cracks are both considered.

The numerical calculation was carried out using the commercial FEM code ABAQUS. Owing to the periodic symmetry of the developed model, a whole structure could be obtained by repeating a periodic pattern along the three axes. Consequently, the macroscopic property could be determined using the periodic pattern with appropriate periodic boundary conditions. Detailed procedure of the periodic boundary condition can be acquired from elsewhere [47]. Herein, all structural units are taken to be homogeneous, isotropic and linear elastic. The Young's modulus and Poisson's ratio of the bulk YSZ are taken as 205 GPa and 0.23 [48], respectively. The bonding between structural units is realized by Tie constraints. In order to obtain the apparent elastic modulus, a uniform displacement is applied on the structure. Subsequently, the stress-strain curve can be obtained from the curve of the reaction force-displacement. The other details to obtain elastic modulus can be found elsewhere [16].

The predicted changes in elastic modulus as a function of duration time are shown in Fig. 11. It can be found that the model prediction exhibit a consistent stage-sensitive evolutionary trends with experimental data. In detail, at the stage-I, the ultra-fast increase of elastic modulus was presented, suggesting that the healing of inter-splat pores is primarily responsible for the structural evolution at this stage. At the stage-II, the evolution of mechanical property was attributed to the healing of connected pore network with much slower kinetic.

Based on the experimental observation and theoretical analysis, it is possible to conclude that the performance degradation induced by

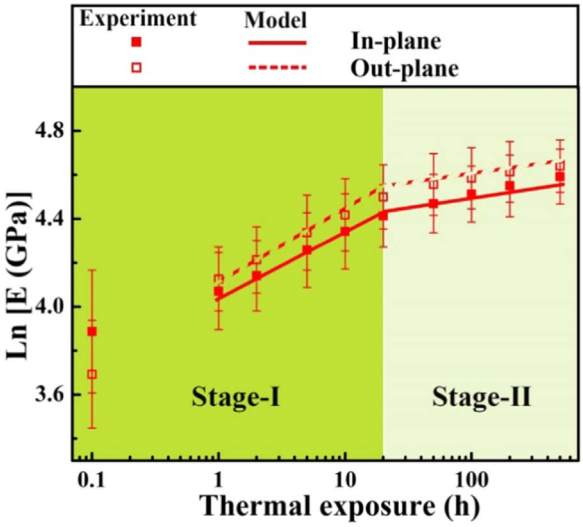

Fig. 11. Comparison between model prediction and experimental results in this study. The data were presented as Ln-t.

sintering is primarily resulted from the healing of inter-splat pores, in particular, at the stage-I. Therefore, in order to retard the sintering kinetic at the stage-I, it would be effective to introduce some in-plane pores with relatively larger scale, and thus the healing through multi-connection would be weakened. It is worth noting that these large pores would inevitable compromise the fracture toughness of the top-coat. Therefore, a detailed work is necessary to balance the performances between thermal insulation and lifetime, so as to realize the structural optimization.

4. Conclusions

A detailed examination on the healing of 2D pores was carried out to investigate the sintering characteristics of the plasma-sprayed TBCs. A structural model was developed to correlate the microstructural evolution with the changes in mechanical property. The detail conclusions are as follows:

(i) The sintering kinetics of the PS-YSZ is highly stage-sensitive. The sintering kinetic at initial short duration (stage-I) is significantly higher than that in the following long duration (stage-II);
(ii) At the stage-I, the ultrafast sintering kinetics is attributed primarily to the healing of the inter-splat pores through multi-connection. This is the unique sintering characteristic of the PS-YSZ. At the stage-II, the slow healing of the inter-splat pores and the intra-splat cracks would proceed through single-connection. This is similar to the conventional ceramic sintering.
(iii) The quantitative correlation between the microstructural evolution and the changes in mechanical property was established. The structural model predicts a stage-sensitive evolution trend in elastic modulus, which is well consistent with experimental data.
(iv) The understanding on sintering behaviour of the TBCs from the 2D pore healing behaviour could provide some directions for structural tailoring of TBCs, in order to achieve high thermal insulation performance.

Acknowledgments

The present project was supported by the National Basic Research Program of China (No. 2013CB035701), the Fundamental Research Funds for the Central Universities, and the National Program for Support of Top-notch Young Professionals.

References

[1] C. Liu, A. Leyland, Q. Bi, A. Matthews, Corrosion resistance of multi-layered plasma-assisted physical vapour deposition TiN and CrN coatings, Surf. Coat. Technol. 141 (2001) 164–173.

[2] B.V. Cockeram, Development of wear-resistant coatings for cobalt-base alloys, Surf. Coat. Technol. 120 (1999) 509–518.

[3] H. Chai, Transverse fracture in thin-film coatings under spherical indentation, Acta Mater. 53 (2005) 487–498.

[4] Y.S. Tian, C.Z. Chen, D.Y. Wang, Q.M. Ji, Recent developments in zirconia thermal barrier coatings, Surf. Rev. Lett. 12 (2005) 369–378.

[5] D. Bernoulli, K. Haefliger, K. Thorwarth, G. Thorwarth, R. Hauert, R. Spolenak, Cohesive and adhesive failure of hard and brittle films on ductile metallic substrates: a film thickness size effect analysis of the model system hydrogenated diamond-like carbon (a-C:H) on Ti substrates, Acta Mater. 83 (2015) 29–36.

[6] N.P. Padture, M. Gell, E.H. Jordan, Materials science - thermal barrier coatings for gas-turbine engine applications, Science 296 (2002) 280–284.

[7] R. Vassen, A. Stuke, D. Stover, Recent developments in the field of thermal barrier coatings, J. Therm. Spray Technol. 18 (2009) 181–186.

[8] C.J. Li, Y. Li, G.J. Yang, C.X. Li, Evolution of lamellar interface cracks during isothermal cyclic test of plasma-sprayed 8YSZ coating with a columnar-structured YSZ interlayer, J. Therm. Spray Technol. 22 (2013) 1374–1382.

[9] A. Ohmori, C.J. Li, Quantitative characterization of the structure of plasma-sprayed Al_2O_3 coating by using copper electroplating, Thin Solid Films 201 (1991) 241–252.

[10] P. Fauchais, M. Fukumoto, A. Vardelle, M. Vardelle, Knowledge concerning splat formation: an invited review, J. Therm. Spray Technol. 13 (2004) 337–360.

[11] A. Cipitria, I.O. Golosnoy, T.W. Clyne, A sintering model for plasma-sprayed zirconia TBCs. Part I: free-standing coatings, Acta Mater. 57 (2009) 980–992.

[12] C.J. Li, A. Ohmori, Relationships between the microstructure and properties of thermally sprayed deposits, J. Therm. Spray Technol. 11 (2002) 365–374.

[13] S. Paul, A. Cipitria, S.A. Tsipas, T.W. Clyne, Sintering characteristics of plasma sprayed zirconia coatings containing different stabilisers, Surf. Coat. Technol. 203 (2009) 1069–1074.

[14] T.W. Clyne, S.C. Gill, Residual stresses in thermal spray coatings and their effect on interfacial adhesion: a review of recent work, J. Therm. Spray Technol. 5 (1996) 401–418.

[15] H. Xie, Y.C. Xie, G.J. Yang, C.X. Li, C.J. Li, Modeling thermal conductivity of thermally sprayed coatings with intrasplat cracks, J. Therm. Spray Technol. 22 (2013) 1328–1336.

[16] G.R. Li, B.W. Lv, G.J. Yang, W.X. Zhang, C.X. Li, C.J. Li, Relationship between lamellar structure and elastic modulus of thermally sprayed thermal barrier coatings with intra-splat cracks, J. Therm. Spray Technol. 24 (2015) 1355–1367.

[17] R.W. Rice, Microstructure Dependence of Mechanical Behaviour of Ceramics, Properties and Microstructure, Academic Press, New York (NY), 1977.

[18] A.L. Loeb, Thermal conductivity: VIII, a theory of thermal conductivity of porous materials, J. Am. Ceram. Soc. 37 (1954) 96–99.

[19] F. Cernuschi, P.G. Bison, S. Marinetti, P. Scardi, Thermophysical, mechanical and microstructural characterization of aged free-standing plasma-sprayed zirconia coatings, Acta Mater. 56 (2008) 4477–4488.

[20] R. Vassen, N. Czech, W. Mallener, W. Stamm, D. Stover, Influence of impurity content and porosity of plasma-sprayed yttria-stabilized zirconia layers on the sintering behaviour, Surf. Coat. Technol. 141 (2001) 135–140.

[21] W.G. Chi, S. Sampath, H. Wang, Microstructure-thermal conductivity relationships for plasma-sprayed yttria-stabilized zirconia coatings, J. Am. Ceram. Soc. 91 (2008) 2636–2645.

[22] B.R. Marple, R.S. Lima, C. Moreau, S.E. Kruger, L. Xie, M.R. Dorfman, Yttria-stabilized zirconia thermal barriers sprayed using N_2-H_2 and Ar-H_2 plasmas: influence of processing and heat treatment on coating properties, J. Therm. Spray Technol. 16 (2007) 791–797.

[23] Y. Tan, J.P. Longtin, S. Sampath, H. Wang, Effect of the starting microstructure on the thermal properties of as-sprayed and thermally exposed plasma-sprayed YSZ coatings, J. Am. Ceram. Soc. 92 (2009) 710–716.

[24] J.A. Thompson, T.W. Clyne, The effect of heat treatment on the stiffness of zirconia top coats in plasma-sprayed TBCs, Acta Mater. 49 (2001) 1565–1575.

[25] R.S. Lima, S.E. Kruger, G. Lamouche, B.R. Marple, Elastic modulus measurements via laser-ultrasonic and Knoop indentation techniques in thermally sprayed coatings, J. Therm. Spray Technol. 14 (2005) 52–60.

[26] S. Guo, Y. Kagawa, Young's moduli of zirconia top-coat and thermally grown oxide in a plasma-sprayed thermal barrier coating system, Scr. Mater. 50 (2004) 1401–1406.

[27] Y. Tan, A. Shyam, W.B. Choi, E. Lara-Curzio, S. Sampath, Anisotropic elastic properties of thermal spray coatings determined via resonant ultrasound spectroscopy, Acta Mater. 58 (2010) 5305–5315.

[28] S.H. Leigh, C.K. Lin, C.C. Berndt, Elastic response of thermal spray deposits under indentation tests, J. Am. Ceram. Soc. 80 (1997) 2093–2099.

[29] H.J. Ratzer-Scheibe, U. Schulz, The effects of heat treatment and gas atmosphere on the thermal conductivity of APS and EB-PVD PYSZ thermal barrier coatings, Surf. Coat. Technol. 201 (2007) 7880–7888.

[30] N. Markocsan, P. Nylen, J. Wigren, X.H. Li, A. Tricoire, Effect of thermal aging on microstructure and functional properties of zirconia-base thermal barrier coatings, J. Therm. Spray Technol. 18 (2009) 201–208.

[31] R. Dutton, R. Wheeler, K.S. Ravichandran, K. An, Effect of heat treatment on the thermal conductivity of plasma-sprayed thermal barrier coatings, J. Therm. Spray Technol. 9 (2000) 204–209.

[32] D.M. Zhu, R.A. Miller, Thermal conductivity and elastic modulus evolution of thermal barrier coatings under high heat flux conditions, J. Therm. Spray Technol. 9 (2000) 175–180.

[33] S.A. Tsipas, I.O. Golosnoy, R. Damani, T.W. Clyne, The effect of a high thermal gradient on sintering and stiffening in the top coat of a thermal barrier coating system, J. Therm. Spray Technol. 13 (2004) 370–376.

[34] G.J. Yang, Z.L. Chen, C.X. Li, C.J. Li, Microstructural and mechanical property evolutions of plasma-sprayed YSZ coating during high-tmperature exposure: comparison study between 8YSZ and 20YSZ, J. Therm. Spray Technol. 22 (2013) 1294–1302.

[35] S. Paul, A. Cipitria, I.O. Golosnoy, L. Xie, M.R. Dorfman, T.W. Clyne, Effects of impurity content on the sintering characteristics of plasma-sprayed zirconia, J. Therm. Spray Technol. 16 (2007) 798–803.

[36] J. Ilavsky, J.K. Stalick, Phase composition and its changes during annealing of plasma-sprayed YSZ, Surf. Coat. Technol. 127 (2000) 120–129.

[37] T. Liu, X.T. Luo, X. Chen, G.J. Yang, C.X. Li, C.J. Li, Morphology and size evolution of interlamellar two-dimensional pores in plasma-sprayed $La_2Zr_2O_7$ coatings during thermal exposure at 1300 °C, J. Therm. Spray Technol. 24 (2015) 739–748.

[38] T. Zhou, P.L. Nie, H.P. Lv, Q.L. Chen, X. Cai, Assessment of elastic properties of coatings by three-point bending and nanoindentation, J. Coat. Technol. Res. 8 (2011) 355–361.

[39] J.F. Li, C.X. Ding, Polishing-induced pull outs of plasma sprayed Cr_3C_2-NiCr coating, J. Mater. Sci. Lett. 18 (1999) 1719–1721.

[40] G.J. Yang, C.J. Li, C.X. Li, K. Kondoh, A. Ohmori, Improvement of adhesion and cohesion in plasma-sprayed ceramic coatings by heterogeneous modification of nonbonded lamellar interface using high strength adhesive infiltration, J. Therm. Spray Technol. 22 (2013) 36–47.

[41] I. Sevostianov, M. Kachanov, Modeling of the anisotropic elastic properties of plasma-sprayed coatings in relation to their microstructure, Acta Mater. 48 (2000) 1361–1370.

[42] F. Kroupa, J. Dubsky, Pressure dependence of Young's moduli of thermal sprayed materials, Scr. Mater. 40 (1999) 1249–1254.

[43] K.A. Erk, C. Deschaseaux, R.W. Trice, Grain-boundary grooving of plasma-sprayed yttria-stabilized zirconia thermal barrier coatings, J. Am. Ceram. Soc. 89 (2006) 1673–1678.

[44] A.J. Shaler, H. Udin, G.C. Kuczynski, M. Bever, Self-diffusion in sintering of metallic particles - discussion, T. Am. I. Min. Met. Eng. 185 (1949) 896–897.

[45] C.J. Li, W.Z. Wang, Quantitative characterization of lamellar microstructure of plasma-sprayed ceramic coatings through visualization of void distribution, Mater. Sci. Eng. A-Struct. 386 (2004) 10–19.

[46] Y. Li, C.J. Li, G.J. Yang, C.X. Li, Relation between microstructure and thermal conductivity of plasma-sprayed 8YSZ coating, Int. J. Mod. Phys. B 24 (2010) 3017–3022.

[47] W.X. Zhang, T.J. Wang, L.X. Li, Numerical analysis of the transverse strengthening behaviour of fiber-reinforced metal matrix composites, Comp. Mater. Sci. 39 (2007) 684–696.

[48] X.J. Lu, P. Xiao, Constrained sintering of YSZ/Al_2O_3 composite coatings on metal substrates produced from eletrophoretic deposition, J. Eur. Ceram. Soc. 27 (2007) 2613–2621.